Layer-dependent Raman spectroscopy study of 3R-phase MoS_2*

CHEN Bingye, JIANG Bin, HUANG Weifeng, LUO Xin

Research Center for Magnetoelectric Physics of Guangdong Province, Key Laboratory of Magnetoelectric Physics and Devices of Guangdong Province, School of Physics, Sun Yat-Sen University, Guangzhou 510275, China

Abstract

Layered transition metal dichalcogenides (TMDs) have attracted extensive interest due to their remarkable electronic, optical, and mechanical properties. Among them, molybdenum disulfide (MoS_2) exhibits two main stacking polytypes: the centrosymmetric 2H phase and the non-centrosymmetric 3R phase. The latter has recently drawn attention for its spontaneous polarization, piezoelectricity, band modulation, and possible topological features, but its lattice dynamics and phonon-related properties remain far less understood. To address this gap, we present a comprehensive study of the layer-dependent Raman phonon characteristics of 3R-phase MoS_2 and systematically compare them with those of the 2H phase. Experimentally, we employed confocal Raman spectroscopy and polarization-resolved second-harmonic generation (SHG) to probe vibrational modes and stacking-dependent nonlinear responses of samples ranging from monolayer to bulk. SHG measurements provided an unambiguous means of distinguishing the stacking orders: while the SHG signal vanishes in even-layer 2H samples due to inversion symmetry, it persists strongly in 3R samples of any thickness. Raman spectra in the low-frequency region revealed distinct shear and breathing modes whose evolution with layer number was analyzed using both the linear chain model (LCM) and the more refined force constant model (FCM). While the LCM qualitatively captures the layer-dependent shifts of interlayer vibrations, the FCM provides quantitative agreement with experiments by explicitly incorporating nearest- and next-nearest-neighbor interactions as well as surface corrections. To further interpret the relative intensities of interlayer Raman modes, we introduced the bond polarization model (BPM), which links mode-dependent scattering strength to the symmetry and orientation of chemical bonds. Our BPM analysis revealed pronounced asymmetry in charge redistribution for 3R stacking, leading to weaker interlayer binding energy compared to 2H (0.111 eV vs. 0.113 eV), and consequently a lower sliding barrier, consistent with the

---

* The paper is an English translated version of the original Chinese paper published in Acta Physica Sinica. Please cite the paper as: **CHEN Bingye, JIANG Bin, HUANG Weifeng, LUO Xin, Layer-dependent Raman spectroscopy study of 3R-phase MoS_2.** *Acta Phys. Sin.*, 2025, 74(22): 226301. DOI: 10.7498/aps.74.20251222

observed propensity of 3R crystals for interlayer slip. In the high-frequency region, both stacking types show characteristic in-plane and out-of-plane modes; however, the peak separation in 3R-phase MoS_2 demonstrates stronger sensitivity to the layer number, making it a more reliable spectroscopic fingerprint for thickness identification. Importantly, we found that surface effects play a critical role in reproducing experimental high-frequency shifts in 3R samples, reflecting their weaker interlayer coupling and enhanced surface contributions. This work establishes a complete picture of the phonon behavior in 3R-phase MoS_2, bridging experiment and theory. Our results demonstrate that Raman spectroscopy combined with SHG provides a powerful toolkit for identifying stacking order and thickness in layered MoS_2. By benchmarking LCM, FCM, and BPM, we clarify the roles of interlayer coupling, stacking symmetry, and surface effects in shaping vibrational properties. These insights not only advance the fundamental understanding of lattice dynamics in non-centrosymmetric TMD polytypes, but also lay the groundwork for exploiting 3R-phase MoS_2 in next-generation optoelectronic, piezoelectric, and quantum devices.

Keywords: 3R-phase MoS_2, linear chain model, force constant model, bond polarization model

PACS：63.20.–e, 63.22.Np, 78.30.–j, 42.65.Ky

doi: 10.7498/aps.74.20251222

cstr: 32037.14.aps.74.20251222

1. Introduction

Transition metal dichalcogenides (TMDs), as typical two-dimensional layered materials, have attracted widespread attention in both fundamental research and device applications because of their outstanding electronic, optical, and mechanical properties. Among them, MoS_2 is one of the most representative materials. Owing to its suitable bandgap and good stability, it has been widely applied in field-effect transistors [1–3], photodetectors, and nonlinear optical devices [4]. In the study of these properties, phonons, as the fundamental excitations of lattice vibrations, not only directly influence thermal transport and optical responses of materials, but also reveal interlayer coupling, structural symmetry, and electronic band characteristics. Therefore, an in-depth investigation of phonon properties is of great significance.

The main experimental techniques for studying phonon properties include neutron scattering, infrared spectroscopy, and Raman spectroscopy. Among them, Raman spectroscopy has become the most commonly used method for investigating phonon behaviors in two-dimensional materials due to its high efficiency, nondestructive nature, and high spatial resolution. Through Raman spectroscopy, the vibrational modes of a material and their layer-

number dependence can be directly obtained, thereby providing crucial information for understanding interlayer interactions and symmetry effects [5].

Among the common stacking configurations, MoS_2 mainly exists in the 2H-phase and the 3R-phase. Compared with the conventional 2H-phase, the 3R-phase possesses a non-centrosymmetric stacking structure and therefore exhibits a series of unique physical properties, including sliding ferroelectricity, piezoelectric effects, band modulation, and potential topological properties [6–9]. These excellent features endow 3R-phase MoS_2 with great potential for applications in emerging optoelectronic and quantum devices, making it an important system worthy of in-depth study. However, existing studies on phonons and Raman spectroscopy of MoS_2 have mainly focused on the 2H-phase, while systematic investigations of the 3R-phase remain relatively limited.

Early studies showed that the linear chain model (LCM) achieved good performance in describing low-frequency modes such as interlayer shear and breathing modes [10–13], but it was inadequate in explaining high-frequency intralayer vibrational modes. Subsequently, the force constant model (FCM) was proposed and has been widely applied. By introducing nearest-neighbor and next-nearest-neighbor interactions at the atomic scale and incorporating surface-effect corrections, it can more accurately describe the layer-dependent evolution of high-frequency peaks [14]. In addition, to further explain the intensity differences among different vibrational modes in Raman scattering, the bond polarization model (BPM) was introduced, and it has demonstrated good applicability in predicting the intensities of shear modes under parallel polarization in the low-frequency region [15]. These theoretical approaches have been successfully applied in studies of 2H-phase MoS_2, but systematic research on the 3R-phase is still lacking.

Based on the above background, this work systematically investigates the phonon properties of 3R-phase MoS_2. By combining Raman spectroscopy experiments with the linear chain model, the force constant model, and the bond polarization model, the layer-dependent evolution of vibrational modes, peak positions, and intensities is analyzed and compared with that of the 2H-phase. Meanwhile, second-harmonic generation signals are employed to effectively distinguish different stacking phases. These studies not only reveal the differences in phonon characteristics between 3R-phase and 2H-phase MoS_2, but also further highlight the important role of Raman spectroscopy in understanding and regulating the physical properties of low-dimensional materials.

2.Methods

In this work, both the Raman spectroscopy and nonlinear second-harmonic generation measurements were carried out at room temperature on mechanically exfoliated samples

transferred onto silicon substrates using a WITec confocal Raman microscope. For the Raman measurements, a 532 nm excitation laser was used, with 10 accumulations, an integration time of 0.5 s, and a laser power of 3 mW. For the nonlinear second-harmonic generation measurements, a 1064 nm excitation laser was employed, with 1 accumulation, an integration time of 0.2 s, and a laser power of 14.24 mW. Polarization-resolved Raman and polarization-resolved nonlinear second-harmonic generation measurements were performed by introducing a polarizer and an analyzer into the optical path.

For the theoretical calculations, the vibrational Raman spectra were calculated using the QUANTUM ESPRESSO package based on density functional theory. Throughout the calculations, norm-conserving (NC) local density approximation (LDA) pseudopotentials were adopted, and the plane-wave energy cutoffs for the wave functions and charge density were set to 75 Ry and 600 Ry, respectively. In modeling the two-dimensional material structures, a vacuum layer of 16 Å was applied along the direction perpendicular to the two-dimensional plane to eliminate spurious interlayer interactions. The energy convergence thresholds for structural optimization and self-consistent calculations were set to 10^{-6} Ry and 10^{-10} Ry, respectively, while the force convergence threshold on each atom was set to 10^{-6} Ry/Bohr. Structural optimization was performed using the Broyden-Fletcher-Goldfarb-Shanno (BFGS) quasi-Newton algorithm, and C_3v symmetry constraints were imposed on both bulk and thin-film systems during the optimization process. For Brillouin-zone sampling, Monkhorst-Pack k-point meshes of 17 × 17 × 5 and 17 × 17 × 1 were employed for the bulk and thin-film systems, respectively. After obtaining the optimized structures and self-consistent wave functions, the Raman intensities were calculated using density functional perturbation theory (DFPT). In the DFPT self-consistent iterations, a mixing factor of 0.2 and a high-precision convergence threshold of 10^{-19} eV were adopted.

3. Results and Discussion

The common structural types of bulk MoS_2 are the 2H-phase and 3R-phase, both of which belong to the hexagonal lattice[16,17]. In essence, both are formed from the 1H phase through different stacking sequences. For the 2H-phase, the atoms in adjacent layers are arranged antiparallel, such that the S atoms and Mo atoms in the upper and lower layers are directly aligned. In contrast, in the 3R-phase, each layer is translated by one bond length relative to the layer below, so that the S atoms in the lower layer are positioned directly beneath the centers of the upper hexagons, while the S atoms in the upper layer are directly above the Mo atoms in the lower layer (Fig. 1(a)). Raman spectroscopy, as a characterization technique based on inelastic light scattering, can reflect the molecular or lattice vibrational modes of materials. Figure 1(b) shows the phonon modes of monolayer MoS_2, in which the in-plane mode is doubly degenerate, and the irreducible representation of the vibrational modes is $\Gamma = 2E' + E'' + A_1' +$

$2A_2''$. The Raman spectra of monolayer, trilayer, and bulk 2H-phase and 3R-phase MoS_2 are shown in Fig. 1(c) and (d), respectively. The main characteristic peaks of the two stacking structures are both located approximately near 383 cm^{-1} and 408 cm^{-1}. The consistency of the spectra for the monolayer samples further indicates that both phases are stacked from the same 1H monolayer structure. The subtle differences between the two phases in the Raman spectra make it difficult to effectively distinguish different stacking phases of MoS_2 using Raman spectroscopy alone.

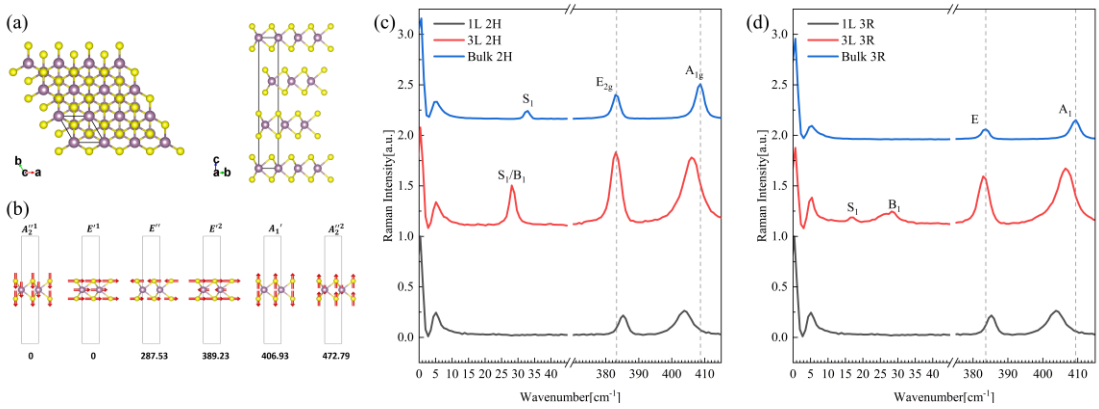

Figure 1. (a) Top view and side view of 3R-phase MoS_2. (b) six phonon modes of monolayer MoS_2, peak positions in cm^{-1}. Raman spectra of (c) 2H-phase and (d) 3R-phase MoS_2 for monolayer, trilayer, and bulk.

Unlike Raman spectroscopy, nonlinear second-harmonic generation (SHG) is highly sensitive to crystal symmetry and therefore can effectively distinguish 2H-phase and 3R-phase MoS_2. As shown in Fig. 2(a) and (b), the 2H-phase retains overall inversion symmetry in even-layer samples, so its SHG signal is significantly weakened or even completely vanishes. By contrast, the 3R-phase lacks inversion symmetry at any thickness and therefore always produces a pronounced SHG response. Based on this property, by measuring the SHG intensity and its evolution with layer number, different stacking phases can be effectively identified, providing a reliable approach for distinguishing the 2H-phase and 3R-phase that are difficult to resolve by Raman spectroscopy[18].

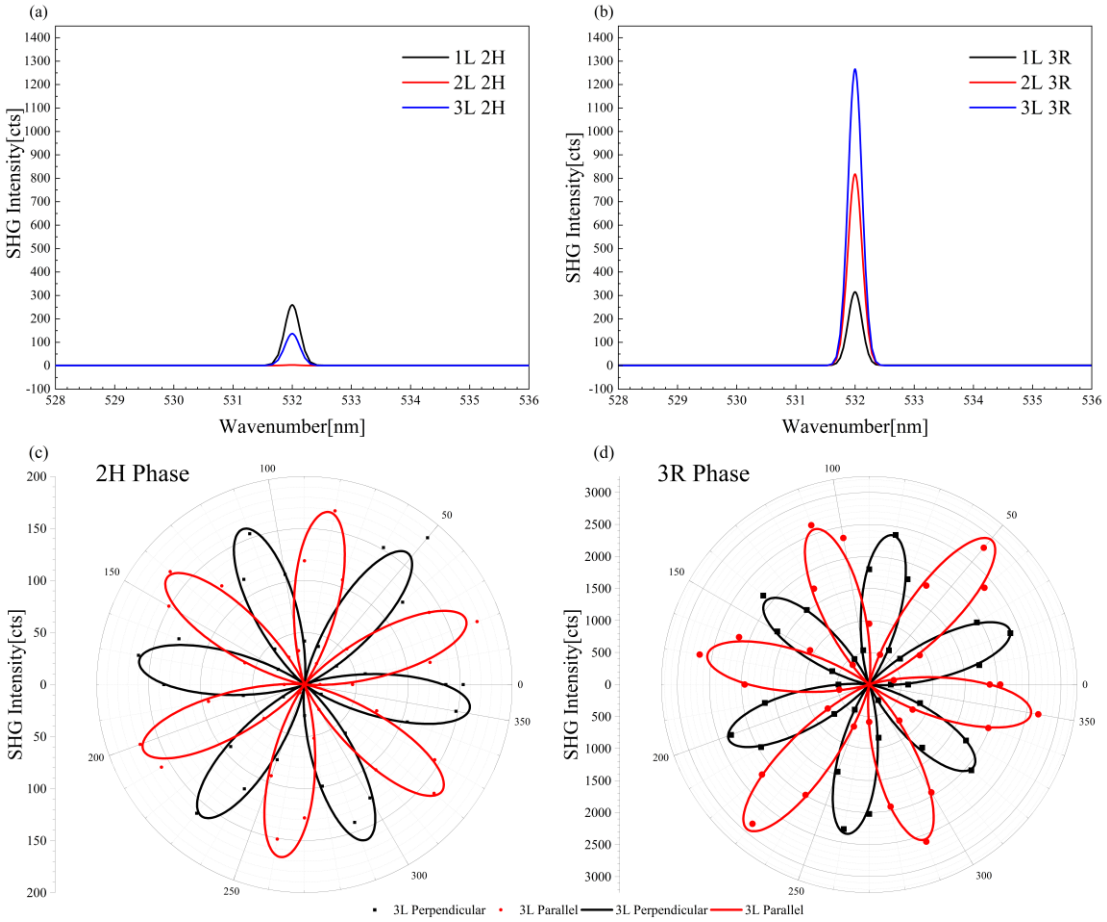

Figure 2. SHG responses of 1–3 layer (a) 2H-phase and (b) 3R-phase MoS_2. polarization SHG polar plots of trilayer (c) 2H-phase and (d) 3R-phase MoS_2.

Furthermore, although the SHG signal of 2H-phase MoS_2 can be observed in odd-layer samples, its intensity gradually decreases as the layer number increases. This phenomenon is mainly attributed to absorption effects: two adjacent oppositely aligned layers can be regarded as a pair whose SHG signals cancel each other, leaving only the residual contribution from the unpaired monolayer. As the layer number increases, the absorption of the excitation light becomes stronger, eventually leading to an overall decay of the SHG intensity[19]. In contrast, the SHG intensity of 3R-phase MoS_2 increases significantly with increasing layer number. A study by Zeng et al. in 2019 showed that this phenomenon originates from the translational offset in the interlayer stacking, which preserves a net in-plane nonlinear dipole moment and gives rise to a nonzero second-order nonlinear susceptibility $\chi^{(2)}$. The nonlinear dipoles from different layers can coherently add, generating a stronger SH field and thus causing the SHG signal to increase monotonically with the layer number[18].

Polarization-resolved second-harmonic generation is an important extension of SHG. By controlling the polarization of the incident light and analyzing the polarization dependence of

the output SHG signal, key information about the material symmetry and crystal-axis orientation can be obtained. For TMD materials, under the parallel-polarization configuration, the SHG intensity satisfies $I_{2\omega} \propto \cos^2(3\varphi + \varphi_0)$, where φ is the angle between the polarization direction of the emitted light $e_{2\omega}$ and the x axis of the sample coordinate system, and φ_0 is the initial angle between the sample coordinate system (x, y) and the laboratory coordinate system (x′, y′). This indicates that the maximum SHG intensity corresponds to the armchair direction of the material. Correspondingly, under the cross-polarization configuration, the intensity satisfies $I_{2\omega} \propto \sin^2(3\varphi + \varphi_0)$, and its maximum corresponds to the zigzag direction of the material[18,20–23]. Because MoS_2 possesses threefold rotational symmetry along the z axis, both 2H-phase and 3R-phase exhibit six-lobed patterns under parallel and cross polarization. Moreover, the relationship between the armchair and zigzag directions causes the six-lobed patterns under the two polarization configurations to differ by 30° and to be complementary to each other (Fig. 2(c) and (d)). It is worth noting that, compared with the symmetric and uniform six-lobed distribution of 2H-phase MoS_2, the 3R-phase exhibits two markedly enhanced lobes under parallel polarization and four enhanced lobes under cross polarization. This originates from the amplified structural asymmetry caused by its staggered stacking configuration[17].

The low-frequency peaks mainly reflect interlayer vibrations, layer-number dependence, and stacking-structure differences, and therefore constitute important spectral features for investigating interlayer interactions in layered materials. Figure 3(a) shows the low-frequency Raman spectra of 2- to 5-layer 2H-phase and 3R-phase MoS_2 under parallel polarization, where the characteristic peaks of both phases are concentrated in the range of 5-50 cm^{-1}. The Raman peaks in this region mainly originate from interlayer shear (S) and breathing (B) vibrations, whereas the intralayer atoms vibrate in phase. For an N-layer two-dimensional material, there are in principle (N−1) interlayer shear modes and (N−1) interlayer breathing modes. The nomenclature of the peak positions is defined as follows: S and B denote the shear and breathing modes, respectively, and the subscripts 0, 1, 2, ..., (N−1) distinguish different branches, where 0 corresponds to the acoustic branch and 1 to (N−1) correspond to the optical branches, with the frequency increasing gradually with the branch index. The experimental results show that, in the low-frequency region, 2H-phase MoS_2 mainly exhibits two characteristic peaks, S_{N-1} and B_1, which undergo a redshift and a blueshift, respectively, with increasing layer number. By contrast, 3R-phase MoS_2 mainly exhibits the S_1 and B_1 peaks, both of which show a redshift with increasing layer number.

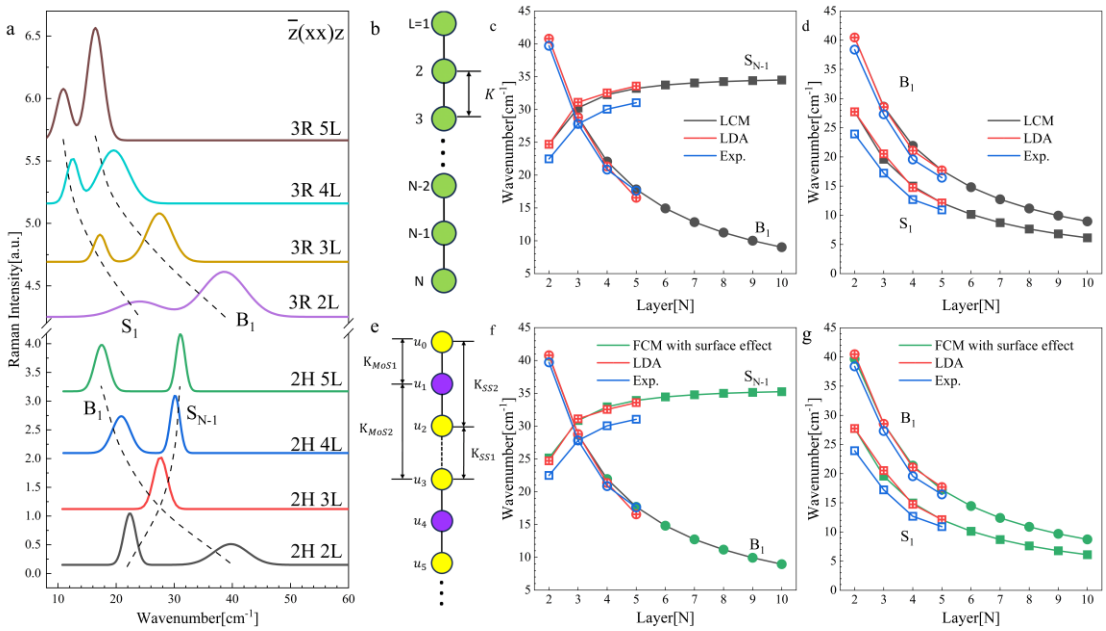

Figure 3. (a) Low-frequency Raman spectra of 2-5 layer 2H-phase and 3R-phase MoS_2 under parallel polarization. (b) Linear chain model. Fitting results of low-frequency peaks for (c) 2H-phase and (d) 3R-phase MoS_2 using the linear chain model. (e) Force constant model. Fitting results of low-frequency peaks for (f) 2H-phase and (g) 3R-phase MoS_2 using the force constant model.

The linear chain model (LCM) can be used to understand and quantitatively describe low-frequency interlayer vibrations in layered materials. In this model, each two-dimensional atomic layer is treated as a rigid unit, and adjacent layers are connected through equivalent force constants, so that the system can be approximated as a one-dimensional atomic chain (Figure 3(b)). By solving the dynamical equations of this simplified system, the analytical frequency relations and displacement relations for the shear and breathing modes can be obtained[13] as follows:

$$u_j^{\alpha} \propto \cos\left[\frac{\alpha(2j-1)\pi}{2N}\right], \tag{1}$$

$$\omega_{\alpha} = \sqrt{\frac{K}{2\mu\pi^2 c^2}\left[1-\cos\left(\frac{\alpha\pi}{N}\right)\right]}, \tag{2}$$

Here, N is the number of layers of the material; u_j^{α} denotes the vibrational displacement of the jth layer (j = 1, 2, ..., N) in the αth vibrational mode (α = 0, 1, 2, ..., N−1, where α = 0 denotes the acoustic branch and the others denote the optical branches); ω_{α} denotes the frequency of the αth vibrational mode, in units of cm^{-1}; μ is the mass per unit area, in units of $kg \cdot m^{-2}$; c is the

speed of light, in units of $cm \cdot s^{-1}$; and K is the force constant of the shear or breathing mode, in units of $N \cdot m^{-3}$[13]. By calculating the frequency of the bilayer system using LDA and substituting it into Eq. (2), the shear and breathing force constants can be back-calculated and further extrapolated to multilayer systems to predict their vibrational modes and frequencies. For MoS_2, the mass per unit area is $\mu = 3.05 \times 10^{-6}\ kg \cdot m^{-2}$. In the 2H-phase, the shear force constant $K_{\parallel}$ is $3.30 \times 10^{19}\ N \cdot m^{-3}$, and the breathing force constant $K_{\perp}$ is $8.99 \times 10^{19}\ N \cdot m^{-3}$; in the 3R-phase, the shear force constant $K_{\parallel}$ is $4.16 \times 10^{19}\ N \cdot m^{-3}$, and the breathing force constant $K_{\perp}$ is $8.85 \times 10^{19}\ N \cdot m^{-3}$.

Figures 3(c) and 3(d) present the predictions of the linear chain model for the low-frequency Raman peaks of 2H-phase and 3R-phase MoS_2. Under the simplified assumptions of the model, the evolution trend of the peak positions with layer number observed experimentally can be reproduced reasonably well, and the results are also consistent with the LDA calculations to a certain extent, thereby validating the rationality of the model. However, because the linear chain model considers only the coupling between adjacent layers and neglects longer-range interactions as well as subtle intralayer structural differences, its description remains simplified.

The force constant model (FCM) is an important extension of the linear chain model. Unlike the linear chain model, which treats each layer as a rigid body and considers only the nearest-neighbor interlayer force constants, the second-order force constant model introduces nearest-neighbor and next-nearest-neighbor force constants at the atomic scale. By describing the second-order linear relationship between atomic displacements and restoring forces, it characterizes the dynamical behavior of the system with higher accuracy and reliability in explaining interlayer vibrational modes and predicting the frequency evolution of different stacking phases. For the MoS_2 system, the second-order force constant model is shown in Figure 3(e), where u_n denotes the displacement of the nth atom. The model contains four types of force constants: K_{MoS1}, K_{SS1}, K_{SS2}, and K_{MoS2}. The subscripts indicate the interacting atomic species, while the numbers 1 and 2 denote nearest-neighbor and next-nearest-neighbor interactions, respectively.

$$-M_n \lambda u_n = \sum_m K_{nm} (u_m - u_n). \tag{3}$$

Table 1 summarizes the experimental frequencies and LDA-calculated results of the vibrational modes of 1H (monolayer), 2H (bulk), and 3R (bulk) MoS_2. Based on the frequencies obtained from the LDA calculations, the force constant model can be further solved to obtain the interatomic force constants. The dynamical equation of the force constant model is given by Eq. (3), where M_n denotes the mass of the nth atom, λ is the square of the frequency ω, u_n is the displacement of the nth atom, and K_{nm} represents the interaction force constant between the

nth and mth atoms.

Table 1. Summary of the force constant values for 3R phase MoS_2.

Phase	Irr. rep.	Exp.	LDA	LDA	Exp.	Irr. rep.	Phase
2H	E_{1u}(I)	—	0	0	—	A_1(I+R)	3R
	A_{2u}(I)	—	0	0	—	E(I+R)	
	E_{2g}(R)	33.29487	35.686900	34.037372	—	E(I+R)	
	B_{1g}	—	57.941155	34.037596	—	E(I+R)	
	E_{2u}	—	285.155367	48.724024	—	A_1(I+R)	
	E_{1g}(R)	—	287.775743	48.724325	—	A_1(I+R)	
	E_{2g}(R)	384.917714	384.976788	285.957612	—	E(I+R)	
	E_{1u}(I)	—	385.716750	285.958139	—	E(I+R)	
	B_{2u}	—	404.033206	290.072680	—	E(I+R)	
	A_{1g}(R)	409.04906	408.106024	385.242202	383.66260	E(I+R)	
	A_{2u}(I)	—	465.182502	386.741898	—	E(I+R)	
	B_{1g}	—	468.960303	386.742311	—	E(I+R)	
1H	E'(I+R)	—	0	405.420245	—	A_1(I+R)	
	A_2''(I)	—	0	405.420515	—	A_1(I+R)	
	E''(R)	—	287.529971	409.217160	409.42571	A_1(I+R)	
	E'(I+R)	385.28101	389.234675	464.326446	—	A_1(I+R)	
	A_1'(R)	403.77329	406.934400	469.500655	—	A_1(I+R)	
	A_2''(I)	—	472.790370	469.501212	—	A_1(I+R)	

Note: I represents infrared activity, R represents Raman activity, and the frequency is in cm^{-1}.

Combined with Figure 1(b), the vibrational modes of monolayer MoS_2 can be decomposed into two classes of displacement relations. Substituting them into the dynamical equation of the force constant model, Eq. (3), the following frequency expressions can be obtained:

Displacement relationship 1 $(u_0 = u_2)$:

$$\lambda_1(E'^1; A_2''^1) = 0, \tag{4}$$

$$\lambda_2(E'^2; A_2''^2) = \frac{K_{MoS1}\,(M_{Mo} + 2M_s)}{M_{Mo}M_s}. \tag{5}$$

Among them, M_{Mo} and M_S denote the atomic masses of Mo and S atoms, respectively.

Displacement relationship 2 $(u_0 = -u_2,\ u_1 = 0)$:

$$\lambda_3(E''; A_1') = \frac{K_{MoS1} + 2K_{SS2}}{M_s}. \tag{6}$$

Similarly, the bulk 3R-phase MoS_2 can be solved in the same manner, and the schematic diagram of its vibrational modes is shown in Figure A1 in Appendix A. Bulk 3R-phase MoS_2 belongs to the C_{3v} symmetry group, and the irreducible representation of its Raman-active vibrational modes is $\Gamma = 9A_1 + 9E$. Unlike 2H-phase MoS_2, some modes in the 3R-phase exhibit near-degeneracy, such as the in-plane modes E^2 and E^3, E^4 and E^5, E^8 and E^9, as well as the out-of-plane modes A_1^2 and A_1^3, A_1^4 and A_1^5, and A_1^8 and A_1^9. Several classes of displacement relations and their corresponding frequency solutions are given below:

Displacement relationship 1: $u_0 = u_2 = u_3 = u_5 = u_6 = u_8$, $u_1 = u_4 = u_7$。

$$\lambda_1(E^1; A_1^1) = 0, \tag{7}$$

$$\lambda_2(E^7; A_1^7) = \frac{(K_{MoS1} + K_{MoS2})(M_{Mo} + 2M_S)}{M_{Mo} M_S}. \tag{8}$$

.

Displacement relationship 2: $u_0 = u_3 = u_6 = -u_2 = -u_5 = -u_8$, $u_1 = u_4 = u_7 = 0$。

$$\lambda_3(E^6; A_1^6) = \frac{K_{MoS1} + K_{MoS2} + 2K_{SS1} + 2K_{SS2}}{M_S}. \tag{9}$$

Displacement relationship 3: $u_6 = -u_0 - u_3$,$u_7 = -u_1 - u_4$,$u_8 = -u_2 - u_5$。

$$\lambda_4(E^2, E^3; A_1^2, A_1^3) = A + \frac{2^{1/3}B}{3 \cdot (C + \sqrt{4B^3 + C^2})^{1/3} M_{Mo} M_s^2} - \frac{(C + \sqrt{4B^3 + C^2})^{1/3}}{3 \cdot 2^{1/3} M_{Mo} M_s^2}, \tag{10}$$

$$\lambda_5(E^4, E^5; A_1^4, A_1^5) = A - \frac{(1 + i\sqrt{3})B}{3 \cdot 2^{2/3} \cdot (C + \sqrt{4B^3 + C^2})^{1/3} M_{Mo} M_s^2} + \frac{(1 - i\sqrt{3})(C + \sqrt{4B^3 + C^2})^{1/3}}{6 \cdot 2^{1/3} M_{Mo} M_s^2}, \tag{11}$$

$$\lambda_6(E^8, E^9; A_1^8, A_1^9) = A - \frac{(1 - i\sqrt{3})B}{3 \cdot 2^{2/3} \cdot (C + \sqrt{4B^3 + C^2})^{1/3} M_{Mo} M_s^2} + \frac{(1 + i\sqrt{3})(C + \sqrt{4B^3 + C^2})^{1/3}}{6 \cdot 2^{1/3} M_{Mo} M_s^2}. \tag{12}$$

Here, A, B, and C are combined parameters composed of atomic masses and force constants, and their explicit forms are given in Eqs. (A1), (A2), and (A3) in Appendix A. It should be noted that the nearly degenerate modes cannot be completely distinguished within the second-order force constant model. When the cubic equation is solved using Cardano's formula, the imaginary unit i appears in the analytical solutions of Eqs. (11) and (12). It should be emphasized that these imaginary terms do not imply the existence of real "imaginary frequencies" or dynamical instability of the system, but merely arise from the formal imperfection of the algebraic analytical expressions. After further simplification, the imaginary parts cancel each other, and the remaining real parts correspond to the physically meaningful frequency squares. In addition, because the various force constants in the same material system differ only slightly, an estimate using the second-order force constants of 2H-phase MoS_2 shows that the imaginary part is about 10^{15} times smaller than the real part and can therefore be completely neglected.

Table 2 presents the force constant coefficients of MoS_2. The values of the force constants are obtained by solving the vibrational frequencies of the bulk and monolayer calculated by LDA, so the subsequent frequency predictions are expected to be close to the LDA results. If sufficient experimental data are available to meet the requirements for solving the force constant model, then a force constant model fitted using experimental values would yield frequency predictions that better match the specific experimental situation. It is worth noting that the values of K_{MoS2} and K_{SS1} for 3R-phase MoS_2 in the table are both larger than those of the 2H-phase. This means that, within the small-displacement approximation around the equilibrium position, the in-plane force-constant coupling in the 3R-phase is stronger, resulting

in higher local stiffness and vibrational frequencies. However, this does not contradict the experimentally observed phenomenon that "3R-phase MoS_2 is more prone to interlayer sliding than the 2H-phase." The reason is that force constants reflect only the local curvature of the system near the equilibrium position, whereas the ease of interlayer sliding is mainly determined by the barrier height of the global sliding potential-energy surface. Because 3R stacking lacks inversion symmetry, the interlayer atomic registry is more relaxed, making the global sliding potential-energy surface flatter and the barrier lower. Therefore, although the 3R-phase exhibits higher coupling stiffness within the local small-amplitude regime, interlayer sliding occurs more easily under large displacements. The detailed derivation and solution procedure of the second-order force constant model for 3R-phase MoS_2 can be found in Appendix A. Furthermore, by substituting the obtained force constants into the dynamical equation of an N-layer system and introducing surface effects through monolayer force constant corrections on the first layer and the Nth layer (see the later discussion for details), the low-frequency peak positions can be predicted. The results are shown in Figure 3. It can be seen that the force constant model is clearly superior to the linear chain model in the accuracy of peak-position fitting, and can accurately describe, at the atomic scale, the combined effects of different stacking configurations, layer-number effects, and surface effects on the vibrational modes.

Table 2. Summary of the force constant values for 3R phase MoS_2.

Force constant type	In-plane mode/ ($N \cdot m^{-1}$)			Out-of-plane mode/ ($N \cdot m^{-1}$)		
	2H block	3 R block	Monolayer	2H block	3 R block	Monolayer
K_{MoS_1}	4.236801	4.21876	4.34525	6.18676	6.15929	6.41101
K_{MoS_2}	0.03023	0.03780	—	0.01955	0.02427	—
K_{SS_1}	0.01571	0.01715	—	0.16477	0.14432	—
K_{SS_2}	–0.188220	–0.18916	–0.19479	0.80216	0.77007	0.75612

Although the force constant model can accurately describe interlayer interactions at the atomic scale and fit the low-frequency vibrational modes reasonably well, it mainly focuses on the vibrational frequencies themselves and remains insufficient for explaining the Raman intensities of the vibrational modes. To further understand the signal strengths of different vibrational modes in Raman scattering, it is necessary to introduce the bond polarization model. The bond polarization model regards the overall polarizability change of a crystal or molecule as the vector superposition of the bond polarizability changes induced by individual chemical

bonds during vibration, thereby explaining and predicting the Raman activity of different vibrational modes through the orientation and symmetry of the bonds. Under the Placzek approximation, the nonresonant Raman intensity is mainly calculated according to Eq. (13), where η and η′ are the unit vectors of the polarization of the incident and scattered light, respectively; R_{ek} is the Raman tensor of the kth vibrational mode; ω_k is the frequency of the kth vibrational mode; $n_k = [\exp(\hbar\omega_k/k_BT) - 1]^{-1}$ is the occupation number; and $P_{\alpha\beta,k} = \Sigma_l[\partial P_{\alpha\beta}/\partial u_{l\gamma}]_0 \chi_{l\gamma}^k$ is the derivative of the electric polarizability tensor $P_{\alpha\beta}$ with respect to the atomic displacement $u_{l\gamma}$. Here, $u_{l\gamma}$ denotes the displacement of the lth atom along the γ direction, i.e., x, y, or z, in the kth vibrational mode, and $\chi_{l\gamma}^k$ is the component of the eigenvector of phonon mode k on the lth atom and along the γ direction[24]

$$I^k \propto \left|\eta \cdot \tilde{R}^k \cdot \eta'\right|^2 \frac{(n_k+1)}{\omega_k} \propto \frac{(n_k+1)}{\omega_k}\left|\sum_{\alpha\beta}\eta_\alpha \eta'_\beta P_{\alpha\beta,k}\right|^2. \tag{13}$$

By simplifying the derivative of the electric polarizability tensor to the xx component, the result shown in Eq. (14) is obtained. Here, $\vec{R}$(l, B) is the bond vector connecting atom l and its nearest-neighbor atom l′ through bond B, and this vector has been normalized to unit length. $\alpha_{\parallel}$ and $\alpha_{\perp}$ represent the static longitudinal and perpendicular bond polarizabilities, respectively, and are assumed to depend only on the bond length R. $\vec{R}_0$(l, B) denotes the bond vector in the equilibrium configuration, normalized to unit length, $R_{0\beta}$ is the β component of $\vec{R}_0$(l, B), and R_0 is the equilibrium bond length. $\alpha'_{\perp}$ and $\alpha'_{\parallel}$ are the radial derivatives of the bond polarizabilities with respect to the bond length[15]

$$P_{xx,k} = -\sum_{lB}\left\{\underbrace{\frac{\alpha'_{//}+2\alpha'_{\perp}}{3}\boldsymbol{R}_0\cdot\boldsymbol{\chi}_l^k}_{\mathrm{I}} + \underbrace{\left(\alpha'_{//}-\alpha'_{\perp}\right)R_{0x}^2\boldsymbol{R}_0\cdot\boldsymbol{\chi}_l^k}_{\mathrm{II}} - \underbrace{\frac{1}{3}\left(\alpha'_{//}-\alpha'_{\perp}\right)\boldsymbol{R}_0\cdot\boldsymbol{\chi}_l^k}_{\mathrm{III}} + \underbrace{2R_{0x}\chi_{lx}^k\frac{\alpha_{//}-\alpha_{\perp}}{R_0}}_{\mathrm{IV}} - \underbrace{2\frac{\alpha_{//}-\alpha_{\perp}}{R_0}R_{0x}^2\boldsymbol{R}_0\cdot\boldsymbol{\chi}_l^k}_{\mathrm{V}}\right\}. \tag{14}$$

Here, we apply the bond polarization model to the low-frequency interlayer shear modes. Figure 4(a) shows the differential charge density distributions of bilayer 2H-phase and 3R-phase MoS_2. A pronounced charge accumulation can be observed in the interlayer region, indicating that the interlayer van der Waals interaction simultaneously exhibits weak covalent characteristics associated with charge transfer and redistribution. The accumulated charge in these bonds can induce dipole moments under an external electric field, and the magnitude of

the induced dipole depends on the bond orientation, i.e., the stacking sequence, thereby affecting the Raman scattering intensity. This also explains the significant effect of stacking order on the Raman intensity observed experimentally. A further comparison shows that the charge distribution in the 3R-phase is markedly asymmetric, whereas that in the 2H-phase is relatively symmetric. This asymmetric charge transfer weakens the uniformity of the interlayer interaction and leads to a reduced interlayer binding energy in the 3R-phase. The calculated binding energy of bilayer 2H-phase MoS_2 is 0.113 eV, whereas that of the 3R-phase is only 0.111 eV. The reduction in binding energy implies a lower barrier energy required for interlayer sliding, and therefore 3R-phase MoS_2 is more prone to interlayer sliding.

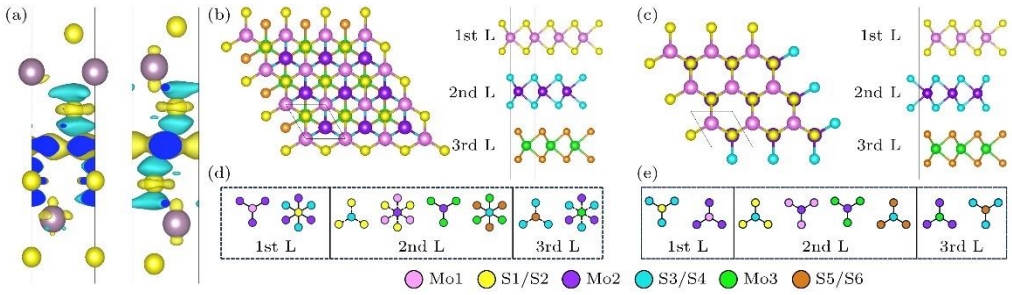

Figure 4. (a) Differential charge density maps of bilayer 3R-phase (left) and 2H-phase (right) MoS_2. Top and side views of trilayer (b) 3R-phase and (c) 2H-phase MoS_2. Bond polarization analysis of trilayer (d) 3R-phase and (e) 2H-phase MoS_2, where dashed lines denote upward bonds and solid lines denote downward bonds. S_i, Mo_i, and S_{i+1} represent the S, Mo, and S atoms in the ith layer from top to bottom, respectively.

We first apply the bond polarization model to trilayer 3R-phase MoS_2 for analysis (Figure 4(b)). Because the low-frequency shear modes are considered, the intralayer atoms vibrate in phase and therefore do not contribute to the change in polarizability; consequently, only the contributions from interlayer atomic bonds need to be considered. For the interlayer shear mode in which each layer moves along the x direction, only χ_{lx}^{k} is nonzero, so that $\vec{R}_0 \cdot \vec{\chi}_l^{k}$ in Eq. (14) should all be replaced by $R_{0x} \cdot \chi_{lx}^{k}$. Equation (14) can thus be simplified as follows:

$$P_{xx,k} = -\sum_{lB} \left[A(r)R_{0x} + B(r)R_{0x}^3\right] \chi_{lx}^{k}, \tag{15}$$

Where both terms are only related to the bond length$r$:

$$A(r) = \frac{\alpha'_{//} + 2\alpha'_{\perp}}{3} - \frac{1}{3}\left(\alpha'_{//} - \alpha'_{\perp}\right) + 2\frac{\alpha_{//} - \alpha_{\perp}}{R_0},$$
$$B(r) = \left(\alpha'_{//} - \alpha'_{\perp}\right) - 2\frac{\alpha_{//} - \alpha_{\perp}}{R_0}.$$

For the first layer, there are three inequivalent atoms, Mo_1, S_1, and S_2. Figure 4(d) presents the bonds between these three inequivalent atomic positions and all atoms in the second layer. Considering all atoms in the first layer, Eq. (16) is obtained.

$$\begin{aligned}
&\sum_{lB} A(r)\chi_{lx}^{k}R_{0x} = A(R_{\mathrm{Mo_1Mo_2}})\Delta_1\left[\frac{a}{R_{\mathrm{Mo_1Mo_2}}}-\frac{a}{2R_{\mathrm{Mo_1Mo_2}}}-\frac{a}{2R_{\mathrm{Mo_1Mo_2}}}\right]+\sum_{i=\{1,2\},j=\{3,4\}} A(R_{\mathrm{S_iS_j}})\\
&\times\Delta_1\left[\frac{a}{R_{\mathrm{S_iS_j}}}-\frac{a}{2R_{\mathrm{S_iS_j}}}-\frac{a}{2R_{\mathrm{S_iS_j}}}\right]+\sum_{i=\{1,2\}} A(R_{\mathrm{S_iMo_2}})\Delta_1\left[-\frac{a}{R_{\mathrm{S_iMo_2}}}+\frac{a}{2R_{\mathrm{S_iMo_2}}}+\frac{a}{2R_{\mathrm{S_iMo_2}}}\right]=0,\\
&\sum_{lB} B(r)\chi_{lx}^{k}R_{0x}^{3} = B(R_{\mathrm{Mo_1Mo_2}})\Delta_1\left[\frac{a^3}{R_{\mathrm{Mo_1Mo_2}}^3}-\frac{a^3}{8R_{\mathrm{Mo_1Mo_2}}^3}-\frac{a^3}{8R_{\mathrm{Mo_1Mo_2}}^3}\right]+\sum_{i=\{1,2\},j=\{3,4\}} B(R_{\mathrm{S_iS_j}})\\
&\times\Delta_1\left[\frac{a^3}{R_{\mathrm{S_iS_j}}^3}-\frac{a^3}{8R_{\mathrm{S_iS_j}}^3}-\frac{a^3}{8R_{\mathrm{S_iS_j}}^3}\right]+\sum_{i=\{1,2\}} B(R_{\mathrm{S_iMo_2}})\Delta_1\left[-\frac{a^3}{R_{\mathrm{S_iMo_2}}^3}+\frac{a^3}{8R_{\mathrm{S_iMo_2}}^3}+\frac{a^3}{8R_{\mathrm{S_iMo_2}}^3}\right]\\
&=\frac{3}{4}a^3\Delta_1\left[\frac{B(R_{\mathrm{Mo_1Mo_2}})}{R_{\mathrm{Mo_1Mo_2}}^3}+\sum_{i=\{1,2\},j=\{3,4\}}\frac{B(R_{\mathrm{S_iS_j}})}{R_{\mathrm{S_iS_j}}^3}-\sum_{i=\{1,2\}}\frac{B(R_{\mathrm{S_iMo_2}})}{R_{\mathrm{S_iMo_2}}^3}\right].
\end{aligned} \tag{16}$$

Here, Δ_i denotes the displacement of the atoms in the ith layer along the x direction, $a = r\sin\lambda$ denotes the projection of bond length r along the x direction, and R_{AB} denotes the bond length of the bond connecting atom A to atom B. It should be noted that, because R_{0x} is the horizontal projection of the bond length, atoms with the same in-plane position but different positions along the z direction, such as Mo_1 and S_3, do not contribute to the Raman intensity under parallel polarization because their bond vectors are oriented along the z axis. As can be seen from Eq. (16), when the specific lattice structure is taken into account, the contribution of the first-order term $\Sigma_{lB}A(r)\chi_{lx}{}^{k}R_{0x}$ to the Raman intensity is zero, and only the third-order term $\Sigma_{lB}B(r)\chi_{lx}{}^{k}R^{3}{}_{0x}$ has a nonzero contribution. Therefore, the first-order term will not be considered further.

For the second layer, there are three inequivalent atoms, Mo_2, S_3, and S_4. We first calculate the bonds associated with the first layer. The left half of the second-layer region in Figure 4(d) presents the bonds between these three inequivalent atomic positions and the atoms in the first layer. Compared with the bonds in the first layer, it may appear that the summation over bonds is duplicated, for example, when the downward bond from Mo_1 to Mo_2 is considered in the first layer and the upward bond from Mo_2 to Mo_1 is then considered in the second layer. The answer can be seen from Eq. (15), in which $\chi_{lx}{}^{k}$ also contains the index l, meaning that even the same bond contributes to the summation of the polarizability change for different layers. Considering all atoms in the second layer, Eq. (17) is obtained.

$$\begin{aligned}\sum_{lB} B(r)\chi_{lx}^{k}R_{0x}^{3} &= B(R_{\mathrm{Mo_2Mo_1}})\Delta_2\left[-\frac{a^3}{R_{\mathrm{Mo_2Mo_1}}^3}+\frac{a^3}{8R_{\mathrm{Mo_2Mo_1}}^3}+\frac{a^3}{8R_{\mathrm{Mo_2Mo_1}}^3}\right]+\sum_{i=\{1,2\},j=\{3,4\}} B(R_{\mathrm{S}_j\mathrm{S}_i}) \\ \times\Delta_2&\left[-\frac{a^3}{R_{\mathrm{S}_j\mathrm{S}_i}^3}+\frac{a^3}{8R_{\mathrm{S}_j\mathrm{S}_i}^3}+\frac{a^3}{8R_{\mathrm{S}_j\mathrm{S}_i}^3}\right]+\sum_{i=\{1,2\}} B(R_{\mathrm{Mo_2S}_i})\Delta_2\left[\frac{a^3}{R_{\mathrm{Mo_2S}_i}^3}-\frac{a^3}{8R_{\mathrm{Mo_2S}_i}^3}-\frac{a^3}{8R_{\mathrm{Mo_2S}_i}^3}\right] \\ =&-\frac{3}{4}a^3\Delta_2\left[\frac{B(R_{\mathrm{Mo_2Mo_1}})}{R_{\mathrm{Mo_2Mo_1}}^3}+\sum_{i=\{1,2\},j=\{3,4\}}\frac{B(R_{\mathrm{S}_j\mathrm{S}_i})}{R_{\mathrm{S}_j\mathrm{S}_i}^3}-\sum_{i=\{1,2\}}\frac{B(R_{\mathrm{Mo_2S}_i})}{R_{\mathrm{Mo_2S}_i}^3}\right].\end{aligned} \tag{17}$$

Considering that the bond length R_{AB} has exchange symmetry (i.e., $R_{\mathrm{AB}}=R_{\mathrm{BA}}$) for the lower index, the third-order terms in the first and second layers can be summed to obtain:

$$\begin{aligned}\sum_{lB} B(r)\chi_{lx}^{k}R_{0x}^{3} &= \frac{3}{4}a^3\Delta_1\left[\frac{B(R_{\mathrm{Mo_1Mo_2}})}{R_{\mathrm{Mo_1Mo_2}}^3}+\sum_{i=\{1,2\},j=\{3,4\}}\frac{B(R_{\mathrm{S}_i\mathrm{S}_j})}{R_{\mathrm{S}_i\mathrm{S}_j}^3}-\sum_{i=\{1,2\}}\frac{B(R_{\mathrm{S}_i\mathrm{Mo_2}})}{R_{\mathrm{S}_i\mathrm{Mo_2}}^3}\right] \\ &-\frac{3}{4}a^3\Delta_2\left[\frac{B(R_{\mathrm{Mo_2Mo_1}})}{R_{\mathrm{Mo_2Mo_1}}^3}+\sum_{i=\{1,2\},j=\{3,4\}}\frac{B(R_{\mathrm{S}_j\mathrm{S}_i})}{R_{\mathrm{S}_j\mathrm{S}_i}^3}-\sum_{i=\{1,2\}}\frac{B(R_{\mathrm{Mo_2S}_i})}{R_{\mathrm{Mo_2S}_i}^3}\right] \\ &=\frac{3}{4}a^3\left[\frac{B(R_{\mathrm{Mo_1Mo_2}})}{R_{\mathrm{Mo_1Mo_2}}^3}+\sum_{i=\{1,2\},j=\{3,4\}}\frac{B(R_{\mathrm{S}_i\mathrm{S}_j})}{R_{\mathrm{S}_i\mathrm{S}_j}^3}-\sum_{i=\{1,2\}}\frac{B(R_{\mathrm{S}_i\mathrm{Mo_2}})}{R_{\mathrm{S}_i\mathrm{Mo_2}}^3}\right](\Delta_1-\Delta_2) \\ &=C_{12}\left(\Delta_1-\Delta_2\right).\end{aligned} \tag{18}$$

Here,C_{12} represents the bond polarization coefficient of the first layer with the second layer:

$$C_{12}=\frac{3}{4}a^3\left[\frac{B(R_{\mathrm{Mo_1Mo_2}})}{R_{\mathrm{Mo_1Mo_2}}^3}+\sum\nolimits_{i=\{1,2\},j=\{3,4\}}\frac{B(R_{\mathrm{S}_i\mathrm{S}_j})}{R_{\mathrm{S}_i\mathrm{S}_j}^3}-\sum\nolimits_{i=\{1,2\}}\frac{B(R_{\mathrm{S}_i\mathrm{Mo_2}})}{R_{\mathrm{S}_i\mathrm{Mo_2}}^3}\right].$$

In the same way, the bond polarization of the second and third layers can be calculated $\sum_{lB} B(r)\chi_{lx}^{k}R_{0x}^{3}=C_{23}(\Delta_2-\Delta_3)$. It should be noted that although the lower index of bond length$R$ is different between C_{12} and C_{23}, the conclusion of $C_{12}=C_{23}=C$ can be drawn by considering the specific stacking structure (Fig. 4(b)). Thus for a 3-layer 3R phase MoS_2,

$$\sum\nolimits_{lB} B(r)\chi_{lx}^{k}R_{0x}^{3}=C(\Delta_1-\Delta_2)+C(\Delta_2-\Delta_3)=C(\Delta_1-\Delta_3),$$

Since C ≠ 0, the term that mainly determines the parallel-polarized low-frequency Raman intensity is $(\Delta_1-\Delta_3)$.

Next, the trilayer 2H-phase MoS_2 is calculated. Figure 4(e) presents the bonds between the three inequivalent atomic positions in the first layer and the atoms in the second layer. Considering all atoms in the first layer gives Eq. (19):

$$\sum_{lB} B(r)\chi_{lx}^{k}R_{0x}^{3} = B(R_{Mo_1Mo_2})\Delta_1\left[-\frac{a^3}{R_{Mo_1Mo_2}^3}+\frac{a^3}{8R_{Mo_1Mo_2}^3}+\frac{a^3}{8R_{Mo_1Mo_2}^3}\right]+\sum_{i=\{1,2\},j=\{3,4\}} B(R_{S_iS_j})$$
$$\times\,\Delta_1\left[\frac{a^3}{R_{S_iS_j}^3}-\frac{a^3}{8R_{S_iS_j}^3}-\frac{a^3}{8R_{S_iS_j}^3}\right]=\frac{3}{4}a^3\Delta_1\left[-\frac{B(R_{Mo_1Mo_2})}{R_{Mo_1Mo_2}^3}+\sum_{i=\{1,2\},j=\{3,4\}}\frac{B(R_{S_iS_j})}{R_{S_iS_j}^3}\right]. \quad (19)$$

Consider all atoms in the second layer and first consider only the bonds associated with the first layer:

$$\sum_{lB} B(r)\chi_{lx}^{k}R_{0x}^{3} = B(R_{Mo_2Mo_1})\Delta_2\left[\frac{a^3}{R_{Mo_2Mo_1}^3}-\frac{a^3}{8R_{Mo_2Mo_1}^3}-\frac{a^3}{8R_{Mo_2Mo_1}^3}\right]+\sum_{i=\{1,2\},j=\{3,4\}} B(R_{S_jS_i})$$
$$\times\,\Delta_2\left[-\frac{a^3}{R_{S_jS_i}^3}+\frac{a^3}{8R_{S_jS_i}^3}+\frac{a^3}{8R_{S_jS_i}^3}\right]=\frac{3}{4}a^3\Delta_2\left[\frac{B(R_{Mo_2Mo_1})}{R_{Mo_2Mo_1}^3}-\sum_{i=\{1,2\},j=\{3,4\}}\frac{B(R_{S_jS_i})}{R_{S_jS_i}^3}\right]. \quad (20)$$

Summing the third-order terms of the first and second layers and considering the exchange symmetry of the index under the bond length, we obtain:

$$\sum_{lB} B(r)\chi_{lx}^{k}R_{0x}^{3} = \frac{3}{4}a^3\Delta_1\left[-\frac{B(R_{Mo_1Mo_2})}{R_{Mo_1Mo_2}^3}+\sum_{i=\{1,2\},j=\{3,4\}}\frac{B(R_{S_iS_j})}{R_{S_iS_j}^3}\right]+\frac{3}{4}a^3\Delta_2\left[\frac{B(R_{Mo_2Mo_1})}{R_{Mo_2Mo_1}^3}\right.$$
$$\left.-\sum_{i=\{1,2\},j=\{3,4\}}\frac{B(R_{S_jS_i})}{R_{S_jS_i}^3}\right]=\frac{3}{4}a^3\left[-\frac{B(R_{Mo_1Mo_2})}{R_{Mo_1Mo_2}^3}+\sum_{i=\{1,2\},j=\{3,4\}}\frac{B(R_{S_iS_j})}{R_{S_iS_j}^3}\right](\Delta_1-\Delta_2)=D_{12}(\Delta_1-\Delta_2). \quad (21)$$

Here, D_{12} represents the bond polarization coefficient of the first layer with the second layer:

$$D_{12}=\frac{3}{4}a^3\left[-\frac{B(R_{Mo_1Mo_2})}{R_{Mo_1Mo_2}^3}+\sum\nolimits_{i=\{1,2\},j=\{3,4\}}\frac{B(R_{S_iS_j})}{R_{S_iS_j}^3}\right].$$

Similarly, the bond polarization between the second and third layers gives $\Sigma_{lB}B(r)\chi_{lx}{}^{k}R^{3}{}_{0x} = D_{23}(\Delta_2-\Delta_3)$. It should be noted that, considering the specific antiparallel stacking structure shown in Figure 4(c), $D_{12} = -D_{23} = D$. Therefore, for trilayer 2H-phase MoS_2,

$$\sum_{lB} B(r)\chi_{lx}^{k}R_{0x}^{3} = D(\Delta_1-\Delta_2)-D(\Delta_2-\Delta_3)$$
$$= D(\Delta_1-2\Delta_2+\Delta_3),$$

Since $D \neq 0$, the term that mainly determines the parallel-polarized low-frequency Raman shear-peak intensity is $(\Delta_1 - 2\Delta_2 + \Delta_3)$.

Using the above results, the model can be generalized to N-layer TMD systems to predict the intensities of the low-frequency shear peaks under parallel polarization. For 3R-phase materials, the intensity is proportional to $C(\Delta_1 - \Delta_N)$; for 2H-phase materials, the intensity is proportional to $D\Sigma_{i=1}{}^{N-1}(\Delta_i - \Delta_{i+1})(-1)^{i+1}$. Using the frequencies obtained from the linear chain model, Eq. (2), and the interlayer displacements, Eq. (1), the peak positions and relative intensities of the low-frequency shear peaks under parallel polarization for 1- to 10-layer systems can be calculated, as shown in Figure 5. In fact, Eqs. (15)-(21) are also applicable to the analysis of breathing modes. The reason why the calculation of the shear modes is taken as an example here is that particular attention is paid to the distinct trends in the layer-number dependence of the shear peaks of 2H-phase and 3R-phase MoS_2 in the low-frequency region.

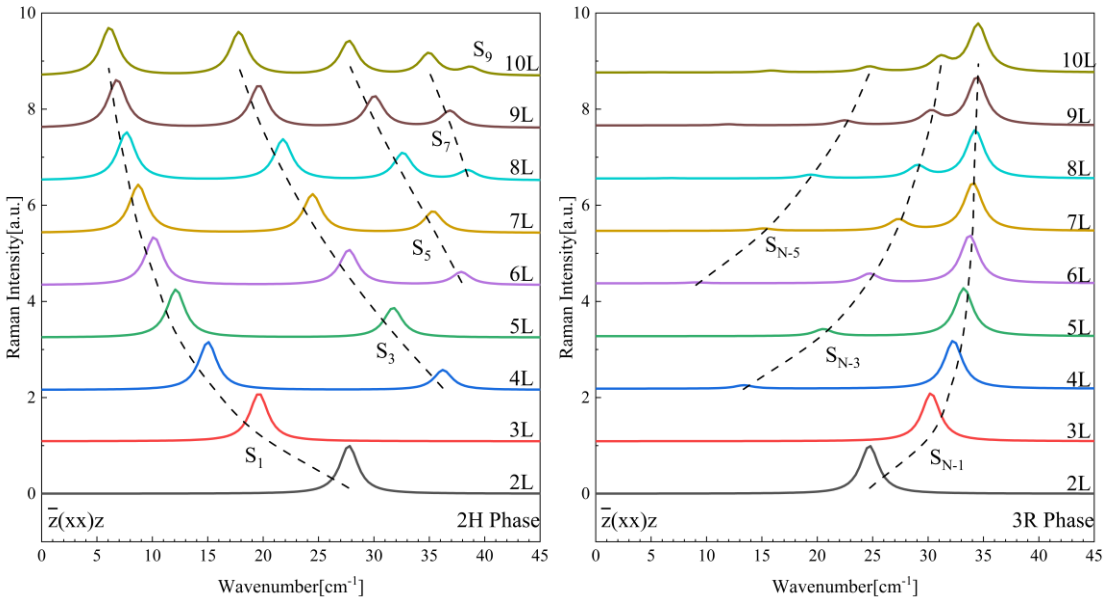

Figure 5. Interlayer Raman intensity maps obtained from the bond polarization model for 2H (left) and 3R (right) stacking configurations.

In 2H-phase MoS_2, the E_{2g} and A_{1g} Raman peaks exhibit a redshift and a blueshift, respectively, with increasing layer number, and their peak separation is often used as a criterion for layer-number identification (Figure 6(a)). By contrast, although the E and A_1 peaks in 3R-phase MoS_2 display a similar layer-dependent behavior (Figure 6(b)), their peak separation responds more significantly to changes in layer number. Therefore, it provides higher sensitivity for layer-number characterization and is of greater practical value than that of the 2H-phase.

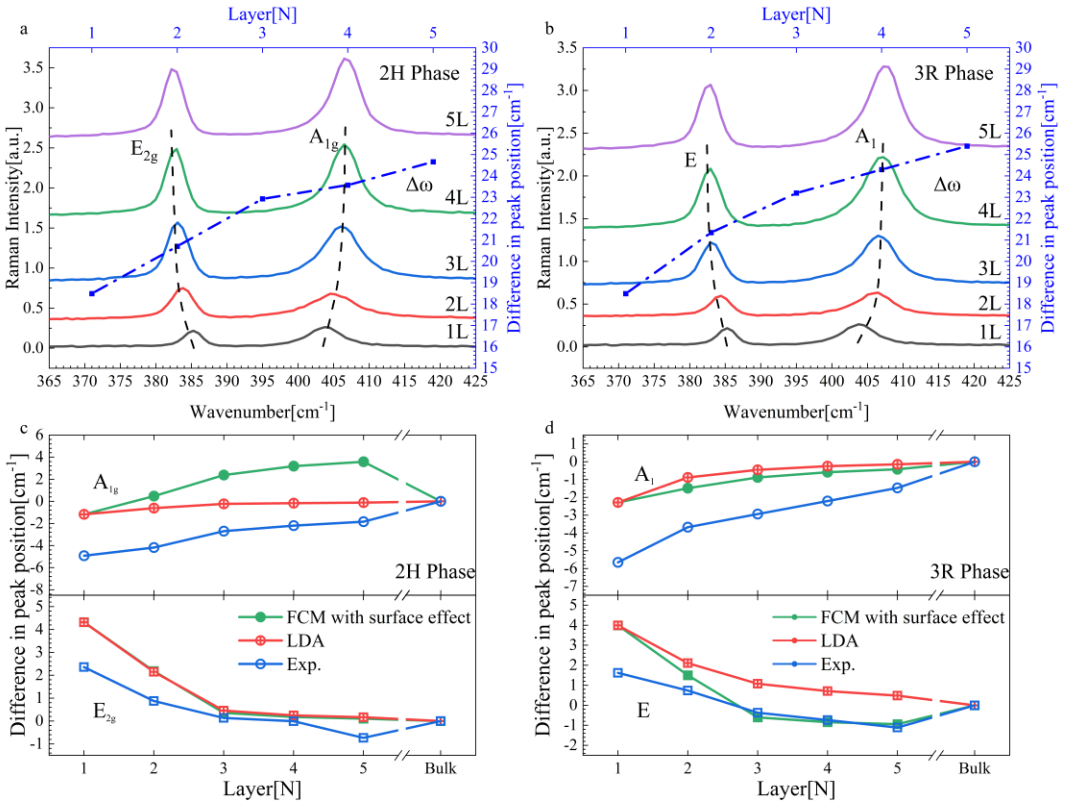

Figure 6. High-frequency peak positions of (a) 2H-phase and (b) 3R-phase MoS_2, together with their peak differences. (c) and (d) show the fitting of high-frequency peak positions using the force constant model with surface effects included, where the peak differences are obtained from the calculated bulk frequencies.

Although the linear chain model has achieved certain success in the study of interlayer vibrational modes, its applicability is limited when describing intralayer vibrational modes. By contrast, the introduction of the force constant model is crucial for addressing this issue. By taking atomic-scale interactions into account, this model can more accurately characterize the dynamical behavior of intralayer vibrational modes. In particular, when surface effects are included, the force constant model can effectively explain the peak-position shifts of the high-frequency modes, thereby demonstrating stronger applicability and higher accuracy.

Surface effects refer to the fact that, in layered materials with a finite number of layers, the outermost atoms lack a symmetric neighboring environment, so that their local force conditions differ from those in the bulk, thereby leading to corrections in the dynamical behavior and vibrational frequencies. In the force constant model, surface effects are usually introduced by modifying the force constants of the two outermost atomic layers, so as to describe the vibrational characteristics of surface atoms when interactions on one side are missing. For an N-layer MoS_2 system, the bond force constant K_{MoS1} that plays the dominant role in the surface region is generally larger, corresponding to a stronger restoring force and a

higher vibrational frequency. As the layer number decreases, the proportion of surface bonds in the whole system increases, which leads to an increase in frequency, namely the so-called surface effect. On the other hand, a decrease in layer number also reduces the interactions within the system, thereby decreasing the accumulated force and lowering the frequency; this is the thickness effect. The competition between these two effects jointly determines the layer-number dependence of the Raman characteristic peaks. For high-frequency in-plane modes, such as the E_{2g} and E modes, surface effects usually dominate, whereas for high-frequency out-of-plane modes, such as the A_{1g} and A_1 modes, the thickness effect is more pronounced[14].

For an N-layer material, the correction to the force constants associated with surface effects is usually implemented by introducing the monolayer MoS_2 force constants into the first and the Nth layers. Figures 6(c) and 6(d) show the peak positions of the two main characteristic peaks of 2H-phase and 3R-phase MoS_2 as functions of layer number. The comparison indicates that, after surface effects are taken into account, the fitted curve of the 3R-phase agrees better with the experimental results. This suggests that surface effects play a more critical role in the simulation of high-frequency phonons in 3R-phase MoS_2. The reason may be that the interlayer coupling is weaker in the 3R stacking configuration, making the influence of the surface layers on the overall vibrational behavior more significant. Therefore, the proper introduction of surface-effect corrections is of great importance for accurately describing the evolution of high-frequency Raman peak positions in 3R-phase MoS_2.

4. Conclusion

In this paper, the Raman phonon properties of 3R phase MoS_2 are systematically studied and compared with those of 2H phase. Raman spectroscopy experiments combined with linear chain model, force constant model and bond polarization model reveal the differences of vibration modes, frequency evolution and intensity selectivity among different stacking modes. The results show that the second harmonic technique can effectively distinguish the stacking phase, the force constant model has higher accuracy in fitting the low and high frequency modes, and the bond polarization model reasonably explains the influence of the stacking structure on the Raman intensity. In addition, the high frequency peak position difference is more sensitive to the layer number change in the 3R phase, highlighting the key role of the surface effect in its phonon behavior. These findings not only provide a new perspective for understanding and controlling the physical properties of 3R phase MoS_2, but also lay an important foundation for the application of low-dimensional materials in optoelectronic devices and quantum devices. In the future, the related research can be further extended to the external field control and non-equilibrium dynamic processes, such as the phonon response under the action of electric field, strain, pressure and optical field, as well as the non-equilibrium phonon evolution and energy relaxation mechanism revealed by ultrafast pump-probe technology, so as to more

comprehensively understand the phonon characteristics of 3R-phase MoS_2, and provide a more solid theoretical and experimental basis for its application in tunable optoelectronic devices, flexible electronics and quantum functional materials.

Appendix A

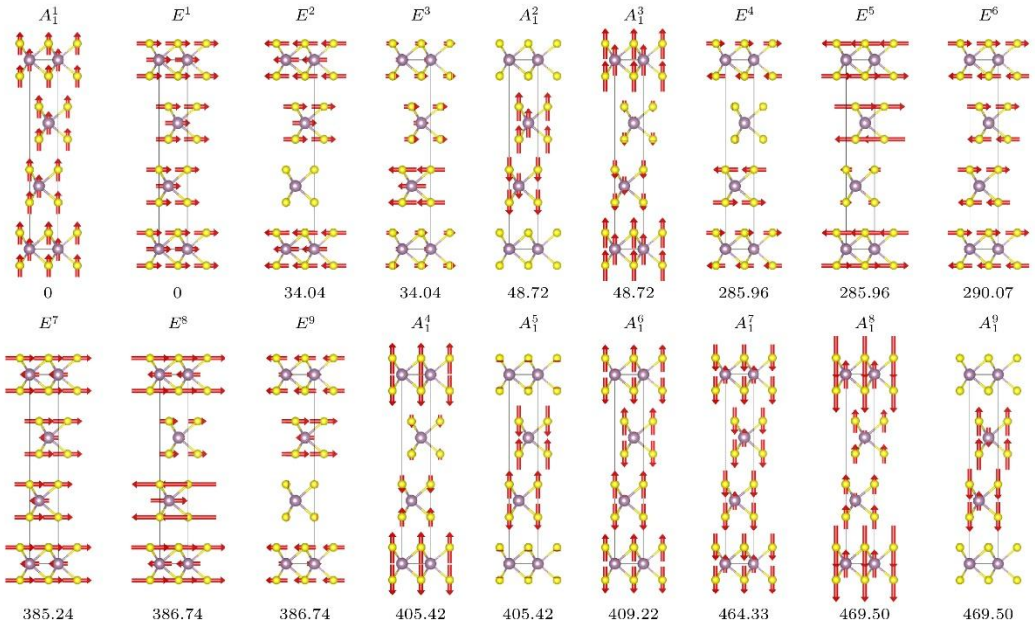

Figure A1. The 18 phonon modes of 3R-phase MoS_2, with peak positions given in cm^{-1}

The frequency eigenvalues are obtained as follows. The various displacement relations are substituted into the dynamical equation of the force constant model and then arranged into the form of homogeneous equations, yielding the corresponding coefficient matrix. According to the number of unknowns, all minors of the same order are selected, and their determinants are set to zero, so that the coefficient matrix is rank-deficient and the homogeneous equations admit nonzero solutions. For displacement relation 3 of bulk 3R-phase MoS_2, the explicit forms of A, B, and C in the resulting frequency expressions, Eqs. (9), (10), and (11), are given as follows:

$$A = \frac{2}{3}\left(\frac{K_{MoS_1} + K_{MoS_2}}{M_{Mo}} + \frac{K_{MoS_1} + K_{MoS_2} + K_{SS_1} + K_{SS_2}}{M_S}\right), \tag{A1}$$

$$\begin{aligned} B = M_S^2\Big(& -4\left[(K_{MoS_1} + K_{MoS_2} + K_{SS_1} + K_{SS_2})M_{Mo} + (K_{MoS_1} + K_{MoS_2})M_S\right]^2 + 3M_{Mo}\Big\{3K_{SS_1}K_{SS_2}M_{Mo} + K_{MoS_1}^2(M_{Mo} + 2M_S) \\ & + K_{MoS_2}^2(M_{Mo} + 2M_s) + 2K_{MoS_2}(K_{SS_1} + K_{SS_2})(M_{Mo} + 2M_S) + 2K_{MoS_1}\left[(K_{SS_1} + K_{SS_2})(M_{Mo} + 2M_S) + K_{MoS_2}(M_{Mo} + 5M_S)\right]\Big\}\Big), \end{aligned} \tag{A2}$$

$$\begin{aligned} C = M_S^3\Big(& -2(K_{SS_1} + K_{SS_2})(8K_{SS_1}^2 - 11K_{SS_1}K_{SS_2} + 8K_{SS_2}^2)M_{Mo}^3 - 6K_{MoS_2}(K_{SS_1} - 2K_{SS_2})(2K_{SS_1} - K_{SS_2})M_{Mo}^2(M_{Mo} - 2M_S) \\ & + 2K_{MoS_1}^3(M_{Mo} - 2M_S)(M_{Mo} + M_S)(M_{Mo} + 4M_S) + 2K_{MoS_2}^3(M_{Mo} - 2M_S)(M_{Mo} + M_S)(M_{Mo} + 4M_S) \\ & + 3K_{MoS_2}^2(K_{SS_1} + K_{SS_2})M_{Mo}(2M_{Mo}^2 - 11M_{Mo}M_S + 8M_S^2) + 6K_{MoS_1}\Big[-(K_{SS_1} - 2K_{SS_2})(2K_{SS_1} - K_{SS_2})M_{Mo}^2(M_{Mo} - 2M_S) \\ & + K_{MoS_2}^2(M_{Mo} - 2M_S)^3 + K_{MoS_2}M_{Mo}\left[2(K_{SS_1} + K_{SS_2})M_{Mo}^2 + (7K_{SS_1} - 20K_{SS_2})M_{Mo}M_S + 8(K_{SS_1} + K_{SS_2})M_S^2\right] \\ & + 3K_{MoS_1}^2\left\{2K_{MoS_2}(M_{Mo} - 2M_S)^3 + M_{Mo}\left[2(K_{SS_1} + K_{SS_2})M_{Mo}^2 + (-11K_{SS_1} + 16K_{SS_2})M_{Mo}M_S + 8(K_{SS_1} + K_{SS_2})M_S^2\right]\right\}\Big). \end{aligned} \tag{A3}$$

A brief description of the procedure for determining the force constants of bulk 3R-phase MoS_2 is given below. From the expression for λ_2, Eq. (8), one obtains

$$K_{MoS_1} + K_{MoS_2} = \frac{\lambda_2 M_{Mo} M_S}{M_{Mo} + 2M_S}. \tag{A4}$$

Substituting (A4) into the expression (9) for λ_3, we obtain

$$K_{SS_1} + K_{SS_2} = \frac{M_S\ (-\lambda_2 M_{Mo} + \lambda_3 M_{Mo} + 2\lambda_3 M_S)}{2\,(M_{Mo} + 2M_S)}. \tag{A5}$$

It can thus be seen that the four force constants are reduced to two independent variables. By further combining the remaining eigenvalue expressions, Eqs. (9), (10), and (11), all force constants can then be completely determined by numerical methods.

References

[1] Radisavljevic B, Radenovic A, Brivio J, Giacometti V, Kis A 2011 Nat. Nanotechnol. 6 147

[2] Mak K F, Lee C, Hone J, Shan J, Heinz T F 2010 Phys. Rev. Lett. 105 136805

[3] Li L, Zhang Y K, Shi D X, Zhang G Y 2022 Acta Phys. Sin. 71 108102

[4] Chhowalla M, Shin H S, Eda G, Li L J, Loh K P, Zhang H 2013 Nat. Chem. 5 263

[5] Jiang B, Ding Y L, Zhao F L, Luo X 2022 Physics and Engineering 32 24

[6] Meng P, Wu Y Z, Bian R J, Pan E, Dong B, Zhao X X, Chen J G, Wu L S, Sun Y Q, Fu Q D, Liu Q 2022 Nat. Commun. 13 7696

[7] Hallil H, Cai W F, Zhang K, Yu P, Liu S, Xu R, Zhu C, Xiong Q H, Liu Z, Zhang Q 2022 Adv. Electron. Mater. 8 2101131

[8] Akashi R, Ochi M, Bordács S, Suzuki R, Tokura Y, Iwasa Y, Arita R 2015 Phys. Rev. Appl. 4 014002

[9] Wu J D, Yang D Y, Liang J, Werner M, Ostroumov E, Xiao Y H, Watanabe K, Taniguchi

T, Dadap J I, Jones D, Ye Z L 2022 Sci. Adv. 8 eade3759

[10] Wieting T 1973 Solid State Commun. 12 931

[11] Luo N, Ruggerone P, Toennies J P 1996 Phys. Rev. B 54 5051

[12] Tan P H, Han W P, Zhao W J, Wu Z H, Chang K, Wang H, Wang Y F, Bonini N, Marzari N, Pugno N 2012 Nat. Mater. 11 294

[13] Zhao Y Y, Luo X, Li H, Zhang J, Araujo P T, Gan C K, Wu J, Zhang H, Quek S Y, Dresselhaus M S, Hua X Q 2013 Nano Lett. 13 1007

[14] Luo X, Zhao Y Y, Zhang J, Xiong Q H, Quek S Y 2013 Phys. Rev. B 88 075320

[15] Luo X, Lu X, Cong C X, Yu T, Xiong Q H, Ying Quek S 2015 Sci. Rep. 5 14565

[16] Van Baren Jeremiah, Ye G H, Yan J An, Ye Z P, Rezaie Pouyan, Yu P, Liu Z, He R, Lui C H 2019 2D Mater. 6 025022

[17] Shi J, Yu P, Liu F C, He P, Wang R, Qin L, Zhou J B, Li X, Zhou J D, Sui X Y 2017 Adv. Mater. 29 1701486

[18] Zeng Z X S, Sun X X, Zhang D L, Zheng W H, Fan X P, He M, Xu T, Sun L, Wang X, Pan A L 2019 Adv. Funct. Mater. 29 1806874

[19] Balla N K, O' brien M, McEvoy N, Duesberg G S, Rigneault H, Brasselet S, McCloskey D 2018 ACS Photonics 5 1235

[20] Li Y L, Rao Y, Mak K F, You Y M, Wang S Y, Dean C R, Heinz T F 2013 Nano Lett. 13 3329

[21] Kumar N, Najmaei S, Cui Q N, Ceballos F, Ajayan P M, Lou J, Zhao H 2013 Phys. Rev. B 87 161403

[22] Malard L M, Alencar T V, Barboza A P M, Mak K F, De Paula A M 2013 Phys. Rev. B 87 201401

[23] Khan A R, Zhang L, Ishfaq K, Ikram A, Yildrim T, Liu B, Rahman S, Lu Y 2022 Adv. Funct. Mater. 32 2105259

[24] Lazzeri M, Mauri F 2003 Phys. Rev. Lett. 90 036401